No. 678 November 2024

Finite Element Simulation for Elastic an Plastic Fluids

M. T. B. Saghir, H. Damanik, S. Turek

ISSN: 2190-1767

Finite Element Simulation for Elastic and Plastic Fluids

Muhammad Tayyab Bin Saghir[a,*], Hogenrich Damanik[a], Stefan Turek[a]

[a]*Institute for Applied Mathematics, LSIII, TU Dortmund University, Vogelpothsweg 87, 44227, Dortmund, Germany.*

Abstract

In this study, we present the development of a 2D finite element solver for simulating fluids exhibiting both elastic and plastic constitutive properties. We achieve this by combining the constitutive models of the Oldroyd-B model for viscoelastic fluids and the Papanastasiou model for Bingham fluids within a single Eulerian numerical framework. Our aim within this approach is to approximate the given velocity, pressure, and elastic stresses. We employ a higher-order finite element method for the velocity-stress approximation and a discontinuous pressure element. This specific element pair has proven highly effective for accurately capturing the behavior of both Oldroyd-B and Bingham fluids, including nonlinear viscosity functions. Our study consists of two main steps. Firstly, we validate the numerical results for each module component of the constitutives to ensure the accuracy of the approximations and calculations. This step is crucial for establishing the reliability and robustness of our approach. Subsequently, in the second step, we apply the solver to simulate elastoviscoplastic fluid behavior in a porous medium. By investigating fluid flow and deformation within this specific context, we aim to demonstrate the capabilities and potential of our methodology.

Keywords: Finite element method, Elastoviscoplastic, Porous media, Oldroyd-B model.

1. INTRODUCTION

Many materials in our everyday life are neither perfectly elastic solids nor simple Newtonian fluids. Efforts to depict such kinds of materials as either solid or fluid often fail; rather, they demonstrate both elasticity and plasticity effects together. The most common example is bread dough. To make bread, you first need to knead the dough. The bread dough experiences the flow under your hand as you knead it; however, when you shape it, it maintains its shape. At this stage, if you gently press your fingertip into the dough it does not spring back, but if you keep kneading the dough for a long time it will then acquire some

*Corresponding author

Email address: msaghir@math.tu-dortmund.de (Muhammad Tayyab Bin Saghir)

elastic properties, and then by doing the poke test it will spring back quickly acting more as an elastic stuff. This dough is not simply a viscoplastic or viscoelastic material but rather elastoviscoplastic because it exhibits viscoplasticity as well as a high degree of elasticity due to the elastic recovery upon the removal of deformation stress. To describe this kind of complex behavior of fluids, recent elastoviscoplastic models have played a vital role. The constitutive properties of such complex fluids usually involve a combination of elastic and plastic behaviors, leading to the development of elastoviscoplastic or viscoelastoplastic fluid models [1, 2]. Numerous models have been proposed to observe such complex fluid behavior [3, 4, 1, 2]. In 2007, Saramito [1] introduced an elastoviscoplastic model, which is a combination of the viscoplastic Bingham and the Oldroyd models, offering an in-depth framework for understanding these materials. The time-independent Saramito model combined with the conservation of momentum and mass reads:

$$\begin{aligned}
\lambda\dot{\boldsymbol{\sigma}} + \max\left(0, \frac{|\boldsymbol{\sigma}_d| - \sigma_y}{|\boldsymbol{\sigma}_d|}\right)\boldsymbol{\sigma} &= 2\eta_m \mathbf{D}(\boldsymbol{u}) \\
\rho\left(\boldsymbol{u}\cdot\nabla\boldsymbol{u}\right) - \operatorname{div}\left(-p\boldsymbol{I} + 2\eta\mathbf{D}(\boldsymbol{u}) + \boldsymbol{\sigma}\right) &= \boldsymbol{f} \\
\nabla\cdot\boldsymbol{u} &= 0 \\
\boldsymbol{u} &= \boldsymbol{u}_\Gamma \quad \text{on} \quad \partial\Omega \\
\boldsymbol{\sigma} &= \boldsymbol{\sigma}_\Gamma \quad \text{on} \quad \partial\Omega
\end{aligned} \tag{1}$$

in (1) $\dot{\boldsymbol{\sigma}}$ reads:

$$\dot{\boldsymbol{\sigma}} = \boldsymbol{u}\cdot\nabla\boldsymbol{\sigma} + \boldsymbol{\sigma}\cdot\mathbf{W}(\boldsymbol{u}) - \mathbf{W}(\boldsymbol{u})\cdot\boldsymbol{\sigma} - a(\boldsymbol{\sigma}\cdot\mathbf{D}(\boldsymbol{u}) + \mathbf{D}(\boldsymbol{u})\cdot\boldsymbol{\sigma}) \tag{2}$$

where λ denotes the relaxation parameter, ρ the density, $\boldsymbol{u}$ the velocity. The solvent and the polymer viscosities are represented by η and η_m respectively. The total viscosity is $\eta_0 = \eta_m + \eta$, $\boldsymbol{f}$ represents the external force, p the pressure. The rate of deformation is $\mathbf{D}(\boldsymbol{u}) = (\nabla\boldsymbol{u} + \nabla\boldsymbol{u}^T)/2$ and the vorticity tensor is represented as $\mathbf{W}(\boldsymbol{u}) = (\nabla\boldsymbol{u} - \nabla\boldsymbol{u}^T)/2$, $\boldsymbol{\sigma}$ represents the stress, σ_y the yield stress and $\boldsymbol{\sigma}_d$ the deviatoric part of the stress $\boldsymbol{\sigma}$ which is represented as:

$$\boldsymbol{\sigma}_d = \boldsymbol{\sigma} - (\operatorname{tr}(\boldsymbol{\sigma})/N)\boldsymbol{I} \tag{3}$$

with N as a spatial dimension, $|\boldsymbol{\sigma}_d| = \sqrt{\operatorname{tr}(\boldsymbol{\sigma}_d\cdot\boldsymbol{\sigma}_d)}$ is the second invariant of deviatoric stress. In (2), a is the material parameter that is associated to the Gordon–Schowalter's derivative [5, 6], $a = 1$ represents the upper convected derivative and $a = -1$ represents the lower convected derivatives. The model represented in (1) behaves as a Kelvin-Voigt viscoelastic solid before yielding and after yielding it behaves as an Oldroyd viscoelastic fluid. Additionally, the model acts as viscoplastic when $\lambda = 0$, while it exhibits viscoelastic properties when $\sigma_y = 0$. In 2008, Saramito presented an improved version of this model [7]. Saramito's work has been influential in offering a clearer framework for studying the

behavior of such complex fluids. In the modeling of such types of equations, the numerical variables depend on the choice of various constitutive models. Many of these constitutive models involve different numerical frameworks to handle the transition between the solid and liquid phases, such as the Saramito model. Although these strategies offer improved accuracy, the numerical treatment becomes significantly more complex, primarily due to the challenges of identifying the interface between the two phases [8]. To address these complexities, we propose a similar approach from Chaparian et al [8, 9]. In our work, we combine the constitutive models of the Oldroyd-B, which has been used as a benchmark for many different numerical techniques [10], and the Papanastasiou regularized model [11] for Bingham fluids within a single Eulerian numerical framework. This strategy, which has recently gained attention in elastoviscoplasticity studies, has demonstrated promising qualitative results.

1.1. Bingham Model

As discussed, our study employs a model to simulate elastoviscoplastic fluids, which combines the Papanastasiou regularized model for Bingham fluids [11] with the Oldroyd-B model [4]. To gain insight from the Papanastasiou model, it's worth examining its fundamentals. Bingham originally introduced the constitutive equation that characterizes viscoplasticity [3]. The Bingham fluid states that below a certain yield stress, there will be no flow, and once that shear yield stress has been exceeded you observe a flow. Mathematically Bingham viscoplastic fluid can be defined as follows:

$$\begin{cases} \mathbf{D}(\boldsymbol{u}) = 0, & \sigma \leq \sigma_y \\ \boldsymbol{\sigma} = \left(\dfrac{\sigma_y}{\mathrm{II}(\mathbf{D})} + \eta_p \right) \mathbf{D}(\boldsymbol{u}), & \sigma > \sigma_y \end{cases} \tag{4}$$

where η_p represents the plastic viscosity. The second invariant of the deformation tensor is defined as:

$$\mathrm{II}(\mathbf{D}) = \sqrt{\mathbf{D} : \mathbf{D}} \tag{5}$$

It is always a challenging task to simulate viscoplastic models. The reason is very obvious by looking into the above presented mathematical model (4) which is divided into two distinct regions. One region is concerned with the no deformation, i.e., $\mathbf{D}(\boldsymbol{u}) = 0$, and the fluid is not yielded, the other region is concerned with the deformation i.e., $\mathbf{D}(\boldsymbol{u}) \neq 0$, and the fluid is yielded. This results in an obvious discontinuity between the two solutions. From the numerical perspective, there is a jump that numerical solvers do not handle, resulting either in slowing a simulation down or causing a divergence. To overcome this difficulty a regularization technique should be implemented. In our work, we are going to implement the Papanastasiou approach [11]:

$$\boldsymbol{\sigma} = \left[\frac{\sigma_y}{\mathrm{II}(\mathbf{D})} (1 - e^{-m\mathrm{II}(\mathbf{D})}) + \eta_p) \right] \mathbf{D}(\boldsymbol{u}) \tag{6}$$

The regularized Papanastasiou model is a widely used framework for modeling Bingham fluids, offering a regularization technique to handle the discontinuous viscosity behavior in

the mathematical model. The idea of the regularization technique is that if the stress goes above or below the yield stress, we expect a smooth function which is ideal for the numerical solver, as there is no discontinuity present in the numerical model. In terms of viscosity, it can be written as:

$$\eta(\mathrm{II}(\mathbf{D})) = \frac{\sigma_y}{\mathrm{II}(\mathbf{D})}\left(1 - e^{-m\mathrm{II}(\mathbf{D})}\right) + \eta_p \tag{7}$$

In (7), m denotes the stress growth parameter also known as the regularization parameter, which needs to be sufficiently large. The advantage of the expression (7) is that it can be used over the whole flow domain, i.e. both yielded and unyielded regions. If the regularization parameter m is large enough the viscosity tends towards η_p [12]. The lower values of m can be used at higher values of yield stress and vice versa [13, 14].

1.2. Papanastasiou Regularized Elastoviscoplastic Model

By incorporating the model presented in (7) into the momentum equation and combining it with the Oldroyd-B model, which captures viscoelastic effects, our approach provides a comprehensive simulation platform for elastoviscoplastic fluids. The steady-state elasto-viscoplastic fluid model combines with the conservation of momentum and mass equation reads:

$$\begin{aligned}
\lambda\left(\boldsymbol{u}\cdot\nabla\boldsymbol{\sigma} - \nabla\boldsymbol{u}\cdot\boldsymbol{\sigma} - \boldsymbol{\sigma}\cdot\nabla\boldsymbol{u}^T\right) + \boldsymbol{\sigma} &= 2\eta_m\mathbf{D}(\boldsymbol{u}) \\
\rho\left(\boldsymbol{u}\cdot\nabla\boldsymbol{u}\right) - \mathrm{div}\left(-p\boldsymbol{I} + 2\eta(\mathrm{II}(\mathbf{D}))\mathbf{D}(\boldsymbol{u}) + \boldsymbol{\sigma}\right) &= 0 \\
\nabla\cdot\boldsymbol{u} &= 0 \\
\boldsymbol{u} &= \boldsymbol{u}_\Gamma \quad \text{on} \quad \partial\Omega \\
\boldsymbol{\sigma} &= \boldsymbol{\sigma}_\Gamma \quad \text{on} \quad \partial\Omega
\end{aligned} \tag{8}$$

In our work the parameter a in (2) is set to $a = 1$ to obtain the Oldroyd-B model, i.e the upper convective derivative and our $\dot{\boldsymbol{\sigma}}$ reads as $\dot{\boldsymbol{\sigma}} = \left(\boldsymbol{u}\cdot\nabla\boldsymbol{\sigma} - \nabla\boldsymbol{u}\cdot\boldsymbol{\sigma} - \boldsymbol{\sigma}\cdot\nabla\boldsymbol{u}^T\right)$, $\eta(\mathrm{II}(\mathbf{D}))$ can be seen in (7).

2. FINITE ELEMENT APPROXIMATION

2.1. Variational Formulation

To obtain the approximate solution to the specified problem in (8), we employ the finite element method [15, 16]. The reason to employ this method is because of its strong mathematical background that has its roots in functional analysis which helps give us all the analysis for the stable nature of the finite element scheme and the well-posedness. The finite element technique starts by formulating the weak form of equation (8). Our objective within this framework is to approximate the velocity, pressure, and elastic stresses in space where we utilize a higher order finite element method for the velocity-stress approximation

and incorporate a discontinuous pressure element. This specific combination of elements has demonstrated exceptional effectiveness in accurately capturing the behavior of both Oldroyd-B and Bingham fluids, including nonlinear viscosity functions [17]. Before presenting the weak form of the problem, let us introduce the Lebesgue and the Sobolev spaces:

$$L^2(\Omega) = \left\{ u : \Omega \to \mathbb{R} \;\middle|\; \int_\Omega |u(x)|^2 \, dx < \infty \right\} \tag{9}$$

$$H^1(\Omega) = \left\{ u \in L^2(\Omega) \;\middle|\; \frac{\partial u}{\partial x_i} \in L^2(\Omega),\ i = 1, \ldots, d \right\} \tag{10}$$

$$H_0^1(\Omega) = \left\{ u \in H^1(\Omega) \;\middle|\; u = 0 \text{ on } \partial\Omega \right\} \tag{11}$$

We introduce the functional spaces $\mathbf{S} := L^2(\Omega)^{d\times d}_{\mathbf{sym}}$, $\mathbf{V} := H_0^1(\Omega)$ and $Q := L^2(\Omega)$ in which stress velocity and pressure reside. The variational form is then derived using the test functions $\boldsymbol{s} \in \mathbf{S}$, $\boldsymbol{v} \in \mathbf{V}$ and $q \in Q$ and then multiply them with equation (8) over the domain Ω with respect to the spatial coordinates $\boldsymbol{x} = (x_1, x_2)$ and do the integration. The weak form is then read as:

To find $(\boldsymbol{u}, \boldsymbol{\sigma}, p) \in \boldsymbol{X} = \mathbf{S} \times \mathbf{V} \times Q$ such that:

$$\begin{aligned}
\int_\Omega \left[\lambda \left(\boldsymbol{u} \cdot \nabla \boldsymbol{\sigma} - \nabla u \cdot \boldsymbol{\sigma} - \boldsymbol{\sigma} \cdot \nabla \boldsymbol{u}^T \right) + \boldsymbol{\sigma} - 2\eta_m \mathbf{D}(\boldsymbol{u}) \right] s \, d\boldsymbol{x} = 0 \quad \forall \quad \boldsymbol{s} \in \mathbf{S} \\
\int_\Omega \left[\rho \left(\boldsymbol{u} \cdot \nabla \boldsymbol{u} \right) - \nabla \cdot \left(-pI + 2\eta(\mathrm{II}(\mathbf{D}))\mathbf{D}(\boldsymbol{u}) + \boldsymbol{\sigma} \right) \right] \boldsymbol{v} \, d\boldsymbol{x} = 0 \quad \forall \quad \boldsymbol{v} \in \mathbf{V} \\
\int_\Omega (\nabla \cdot \boldsymbol{u}) q \, d\boldsymbol{x} = 0 \quad \forall \quad q \in Q
\end{aligned} \tag{12}$$

Further integrating by parts yields:

$$\begin{aligned}
\int_\Omega \left[\lambda \left(\boldsymbol{u} \cdot \nabla \boldsymbol{\sigma} - \nabla \boldsymbol{u} \cdot \boldsymbol{\sigma} - \boldsymbol{\sigma} \cdot \nabla \boldsymbol{u}^T \right) + \boldsymbol{\sigma} - 2\eta_m \mathbf{D}(\boldsymbol{u}) \right] \boldsymbol{s} \, d\boldsymbol{x} = 0 \quad \forall \quad \boldsymbol{s} \in \mathbf{S} \\
\int_\Omega \left[\rho (\boldsymbol{u} \cdot \nabla \boldsymbol{u} \right] \boldsymbol{v} \, d\boldsymbol{x} - \int_\Omega \left[(-p\boldsymbol{I} + 2\eta(\mathrm{II}(\mathbf{D}))\mathbf{D}(\boldsymbol{u}) + \boldsymbol{\sigma}) \right] \nabla \boldsymbol{v} \, d\boldsymbol{x} = 0 \quad \forall \quad \boldsymbol{v} \in \mathbf{V} \\
\int_\Omega (\nabla \cdot \boldsymbol{u}) q \, d\boldsymbol{x} = 0 \quad \forall \quad q \in Q
\end{aligned} \tag{13}$$

Introducing here a pair of finite-dimensional approximation spaces $\mathbf{S}_h = \mathrm{span}\{\chi_1, \ldots, \chi_Z\}$, $\mathbf{V}_h = \mathrm{span}\{\psi_1, \ldots, \psi_N\}$ and $Q_h = \mathrm{span}\{\varphi_1, \ldots, \varphi_M\}$. The discretized solution is decomposed as follows:

$$\boldsymbol{u}_h = \sum_{i=1}^{N} \boldsymbol{u}_i \psi_i, \quad p_h = \sum_{j=1}^{M} p_j \phi_j, \quad \boldsymbol{\sigma}_h = \sum_{k=1}^{Z} \boldsymbol{\sigma}_k \chi_k \tag{14}$$

finally, the discrete system of equations to be solved can be expressed as a typical saddle-point problem:

$$\begin{pmatrix} \mathcal{F} & \mathcal{M} & \mathcal{B} \\ \mathcal{H} & \mathcal{L} & 0 \\ \mathcal{B}^T & 0 & 0 \end{pmatrix} \begin{pmatrix} \boldsymbol{u} \\ \boldsymbol{\sigma} \\ p \end{pmatrix} = \begin{pmatrix} r_u \\ r_\sigma \\ r_p \end{pmatrix} \tag{15}$$

with

$$\begin{aligned}
\mathcal{F} = f_{ij} &= \int_\Omega \left(\rho \psi_j \nabla \psi_j - 2\eta_s \mathbf{D}(\psi_j)\right) : \mathbf{D}(\psi_i)\, d\boldsymbol{x} \quad \forall\, i,j = 1,\dots,N \\
\mathcal{M} = m_{ij} &= \int_\Omega \chi_j : \mathbf{D}(\psi_i)\, d\boldsymbol{x} \quad \forall\, i = 1,\dots,N,\ j = 1,\dots,Z \\
\mathcal{B} = b_{ij} &= \int_\Omega \phi_j \nabla \cdot \psi_i\, d\boldsymbol{x} \quad \forall\, i = 1,\dots,N,\ j = 1,\dots,M \\
\mathcal{H} = h_{ij} &= \int_\Omega \left(-2\eta_m \mathbf{D}(\psi_j)\right) : \mathbf{D}(\chi_i)\, d\boldsymbol{x} \quad \forall\, i = 1,\dots,Z,\ j = 1,\dots,N \\
\mathcal{L} = l_{ij} &= \int_\Omega \lambda \left((\psi_k \cdot \nabla)\, \chi_j - \nabla \psi_k \cdot \chi_j - \chi_j \cdot \nabla \psi_k^T + \chi_j \right) \chi_i\, d\boldsymbol{x} \\
&\qquad \forall\, i,j = 1,\dots,Z,\ k = 1,\dots,N
\end{aligned} \tag{16}$$

In the context of the finite element method (FEM) applied to (13), the choice of spaces for velocity, pressure, and stress variables is crucial for achieving accurate and stable numerical solutions. The selection of these spaces is motivated by various considerations, including the mathematical properties of the problem, the desired accuracy of the approximation, and computational efficiency. In particular choice of the above finite-dimensional spaces for velocity and pressure is subjected to the LBB condition [18], where its discrete version reads:

$$\sup_{\boldsymbol{u} \in \mathbf{V}_h} \frac{\int_\Omega (\nabla \cdot \boldsymbol{u}) q\, d\boldsymbol{x}}{\|\boldsymbol{u}\|_{1,\Omega}} \geq \alpha \|q\|_{0,\Omega} \quad \forall \quad q \in Q_h \tag{17}$$

Concerning the approximated spaces $\mathbf{V}_h$ and $\mathbf{S}_h$ a similar kind of condition has been studied

in [10] and this is subjected to more complex analysis

$$\sup_{\boldsymbol{\sigma}\in\mathbf{S}_h} \frac{\int_\Omega (\nabla\cdot\boldsymbol{\sigma})\boldsymbol{u}\,d\boldsymbol{x}}{\|\boldsymbol{\sigma}\|_{0,\Omega}} \geq \gamma\|\boldsymbol{u}\|_{1,\Omega} \quad \forall \quad \boldsymbol{u}\in\mathbf{V}_h \tag{18}$$

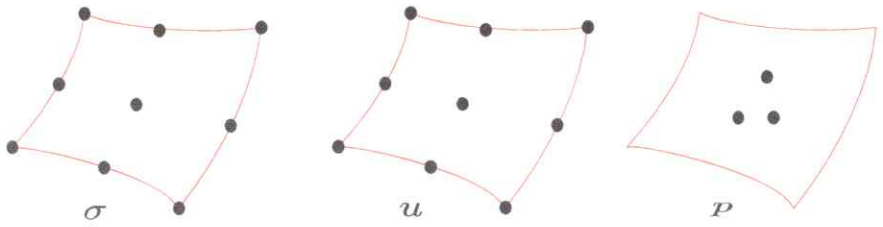

Figure 1: Q_2/P_1 element for velocity/stress and pressure.

To achieve high accuracy and efficiency in approximating $(\boldsymbol{\sigma}, \boldsymbol{u}, p)$, we discretize the solutions in the following discrete spaces:

$$\mathbf{S}_h = \{\boldsymbol{s}_h \in \mathbf{S} \mid \boldsymbol{s}_{h|T} \in (Q_2(T))^{2\times 2} \text{ for all } T \in \mathcal{T}_h\} \tag{19}$$

$$\mathbf{V}_h = \{\boldsymbol{v}_h \in \mathbf{V} \mid \boldsymbol{v}_{h|T} \in (Q_2(T))^2 \text{ for all } T \in \mathcal{T}_h, \boldsymbol{v}_{h|\partial\Omega_h} = 0\} \tag{20}$$

$$Q_h = \{q_h \in Q \mid q_{h|T} \in P_1(T) \text{ for all } T \in \mathcal{T}_h\} \tag{21}$$

2.2. Numerical Solver

The system of the equations represented in (15) is then solved using the Newton-Raphson method [19] by setting $R(\boldsymbol{x}) = 0$, where $R = (\boldsymbol{u}, \boldsymbol{\sigma}, p)$. This method is known for its robustness in solving the nonlinear systems of equations. However, it does have some limitations. One significant drawback is the computational cost associated with forming and inverting the Jacobian matrix, especially for large systems. Additionally, finding an appropriate initial guess that leads to convergence can be challenging. To address these challenges and enhance the method's efficiency, various strategies can be employed. One approach is to use a line search method and an optimal damping factor is calculated for the outer iteration:

$$\boldsymbol{x}^{n+1} = \boldsymbol{x}^n + \omega^n \left[\frac{\partial R(\boldsymbol{x}^n)}{\partial \boldsymbol{x}^n}\right] R(\boldsymbol{x}^n) \tag{22}$$

such that $R(\boldsymbol{x}^{n+1})\cdot\boldsymbol{x}^{n+1} \leq R(\boldsymbol{x}^n)\cdot\boldsymbol{x}^n$, which helps stabilize the convergence and can reduce the computational time required for convergence. Furthermore, instead of computing the exact Jacobian matrix, an approximation can be used to reduce the computational burden. The finite difference method, particularly the divided difference method, is commonly employed to approximate the Jacobian matrix [20]. This approximation provides a reasonable estimate of the Jacobian without the need to compute the exact derivatives analytically.

By incorporating these strategies, the Newton-Raphson method can be made more efficient and practical for solving large-scale nonlinear systems of equations, addressing some of its inherent limitations.

3. Numerical Results

In the numerical analysis section, we thoroughly investigate and validate our mathematical formulations and establish the performance and authentication of our solver. We first begin with the numerical validation of the viscoplastic component by simulating unidirectional flow within a channel. Following this, our focus will be to validate the viscoelastic properties of the fluid. For this purpose, we are going to perform the benchmark simulations for the flow around a cylinder. Lastly, we will check the credibility of the elastoviscoplastic component by conducting simulations based on a porous media benchmark for symmetric and unsymmetric parts.

3.1. Validating Bingham Part

This section is concerned with the validation of the viscoplastic part of our model by considering a unidirectional flow in a unit square channel and also figuring out the insights of the regularization parameter m by computing the errors for different values of m.

3.1.1. Dirichlet Boundary Condition

The initial validation case focuses on validating the viscoplastic component described by (8). In this assessment, we exclude the relaxation parameter and the polymer viscosity terms to identify the viscoplastic behavior. In this part, we analyze a unit square domain. The velocity field in a channel flow is given by

$$u_x = u(y) \quad u_y = 0 \tag{23}$$

and is supposed to occur between two parallel plates separated by distance h. The analytical solution for this specific problem is referenced in the literature [21, 22, 23, 24].

$$[u_x, 0]^T = u\,(y) = \begin{cases} \dfrac{1}{8}\{(1-2\sigma_y)^2 - (1-2\sigma_y-2y)^2\} & 0 \le y < \dfrac{1}{2} - \sigma_y \\ \dfrac{1}{8}(1-2\sigma_y)^2 & \dfrac{1}{2} - \sigma_y \le y \le \dfrac{1}{2} + \sigma_y \\ \dfrac{1}{8}\{(1-2\sigma_y)^2 - (2y-2\sigma_y-1)^2\} & \dfrac{1}{2} + \sigma_y < y \le 1 \end{cases} \tag{24}$$

The rigid (or the plug) region lies in the region $y \in [1/2 - \sigma_y, 1/2 + \sigma_y]$ and moving at a constant velocity, the distance between the parallel plates is considered to be 1. Dirichlet conditions in terms of analytical solution are applied at the left and right walls, and the no-slip condition is set on the upper and lower walls. In this simulation, we set the yield stress value to be $\sigma_y = 0.25$ and iterate over a different range of the regularization parameter m

and the refinement levels. A creeping flow is considered in the simulations by setting $\rho = 0$. Furthermore, comprehensive calculations are carried out to assess the results obtained.

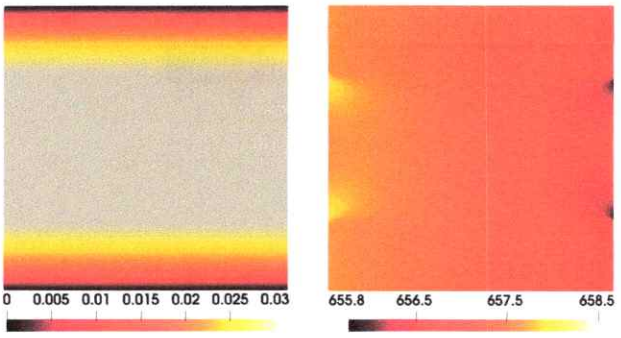

(a) Velocity magnitude (b) Pressure

Figure 2: Visualization of velocity magnitude and pressure distribution at $\sigma_y = 0.25$.

Table 1: The relationship between the L-2 norm velocity error and the regularization parameter m observed at different refinement levels.

	2	3	4	5	6
$m = 10^1$	$2.83182e-3$	$2.80536e-3$	$2.80385e-3$	$2.80802e-3$	$2.80380e-3$
$m = 10^2$	$4.77711e-4$	$5.54487e-4$	$5.35859e-4$	$5.35504e-4$	$5.35404e-4$
$m = 10^3$	$7.95147e-5$	$8.09976e-5$	$9.17084e-5$	$8.69674e-5$	$8.48112e-5$
$m = 10^4$	$8.67548e-6$	$8.83069e-6$	$8.97524e-6$	$9.33456e-6$	$9.88019e-6$
$m = 10^5$	$8.75649e-7$	$8.98809e-7$	$9.23477e-7$	$9.52896e-7$	$9.71171e-7$

The error reduction presented in Table 1 is influenced by the choice of the regularization parameter m, an increase in the number of regularization parameters leads to a substantial decrease in the error. It is evident from the above table that the larger values of m result in a significant reduction of the error and help capture the true behavior of viscoplastic fluids.

3.1.2. Pressure Gradient

A linear pressure is a solution to equations (8), with the corresponding Bingham constitutive relation in equation (6). However, the pressure field in Figure 2 shows a discontinuity in the region around the rigid zone. This lack of smoothness arises because, within the Bingham constitutive model, alternative pressure solutions may exist in the unyielded region, which in this case lies in the central area. The remedy is straightforward: a pressure difference between inflow and outflow is imposed along the inflow or outflow boundaries, such that $u_y = 0$ and $\boldsymbol{\sigma} \cdot \boldsymbol{n} = 0$ in the outward normal direction of the numerical domain. This approach smooths the pressure distribution, as shown in Figure 3.

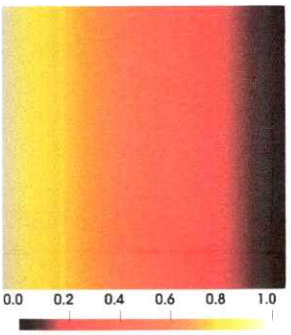

Figure 3: Visualization of a smooth pressure field.

3.2. Validating Viscoelastic Part

3.2.1. Planar Flow Past a Cylinder

Upon successfully validating the viscoplastic component, our subsequent focus shifts to validate the viscoelastic component by setting the yield stress, σ_y, to zero in (8). To validate the viscoelastic component, we selected the flow around a cylinder benchmark to investigate drag across different Weissenberg numbers. Despite having no singularities in the geometry of the flow around a cylinder, achieving convergence at high elasticity is always a challenging task.

3.2.2. Problem Description

The computational domain under consideration for this benchmark problem consists of a rectangular region with a centrally located semi-circular cylinder. We considered the half domain in our simulations due to the symmetric problem. The domain spans a length along the x-axis ranging from $x \in [-20, 20]$, and a height along the y-axis from $y \in [a, b] = [0, 2]$. Within this domain, a centrally located semi-circular cylinder has a radius $r = 1$. The ratio between H (channel height) and r is to be considered as 2 or simply $H = 2r$. A visual representation of this geometry is illustrated in the accompanying figure. This setup serves as the basis for our viscoelastic validation study. Concerning the boundary conditions, a

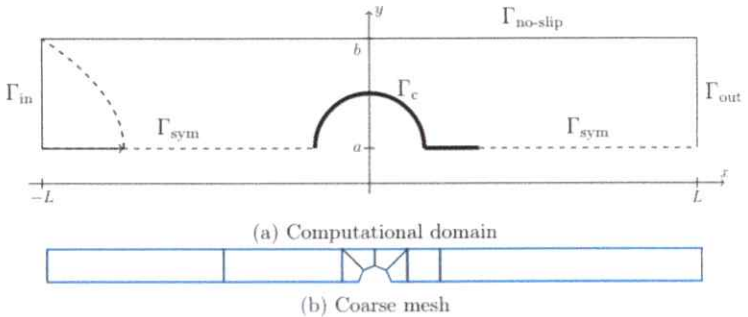

(a) Computational domain

(b) Coarse mesh

Figure 4: Flow around cylinder coarse mesh (half of the domain).

fully developed velocity profile is specified at the inlet and outlet, aiming for a mean velocity

of $U_{\text{mean}} = 1.0$. For the Oldroyd-B model, the corresponding parabolic profile at the inlet is expressed as:

$$u_x = \frac{3}{2} U_{\text{mean}} \left(1 - \left(\frac{y}{H}\right)^2\right), \quad u_y = 0 \tag{25}$$

The upper and lower walls are defined as no-slip boundaries in terms of velocity. The dimensionless parameters governing the problem are the Weissenberg number $We = \lambda U/r$ and the viscosity ratio $\beta = \eta/\eta_0$, where $U = 1$. In this study, the viscosity ratio β is set to be 0.59, $\eta_m = 1$ to have resemblance with the other benchmarks [25, 26, 27]. A creeping flow is considered in the simulations by setting $\rho = 0$. The drag coefficient is calculated over the surface of a cylinder with the help of the following expression:

$$C_{\text{drag}} = 2 \int_s (\boldsymbol{\sigma} \cdot \boldsymbol{n})\, ds \tag{26}$$

Our focus lies on determining the drag coefficient on the cylinder surface for various relaxation times. A strong agreement between our computational results and the reference findings [26] affirms the accuracy of our numerical implementation. More accuracy can be obtained by increasing the mesh refinement. NI represents the number of iterations in the below table.

	We= 0.1			**We**= 0.2		
Level	**Drag**	**NI**	**Ref.** [26]	**Drag**	**NI**	**Ref.** [26]
3	130.063	3	-	126.361	3	-
4	130.283	3	-	126.551	3	-
5	130.342	3	130.366	126.606	3	126.628
	We= 0.3			**We**= 0.4		
Level	**Drag**	**NI**	**Ref.** [26]	**Drag**	**NI**	**Ref.** [26]
3	122.969	3	-	120.416	3	-
4	123.105	3	-	120.527	3	-
5	123.171	3	123.194	120.572	3	120.593
	We= 0.5			**We**= 0.6		
Level	**Drag**	**NI**	**Ref.** [26]	**Drag**	**NI**	**Ref.** [26]
3	118.730	4	-	117.730	4	-
4	118.766	4	-	117.717	4	-
5	118.809	4	118.828	117.758	4	117.779

Table 2: Validation of the solver against drag values of the flow over a cylinder in a rectangular channel for different Weissenberg numbers and $\beta = 0.59$.

3.3. Validating Elastoviscoplastic Part

In the final phase of our validation process, we will evaluate the elastoviscoplastic component by examining its behavior. For this, we will perform our simulations in a porous media as a test case [9]. This particular test case serves as a comprehensive benchmark to evaluate the performance and accuracy of our mathematical formulations.

3.3.1. Flow in Porous Media

Studying the dynamics of the fluid that flows through porous media is of great importance in many fields of engineering, and natural science, including other areas such as soil sciences, hydrology, solid mechanics, and polymer property measurement[28, 29]. The purpose of this study is to investigate the complex fluid possessing elastic, viscous, and plastic properties through the porous media. Flow of complex fluid, in our case elastoviscoplastic, materials through porous media has been the key interest for many researchers. By considering the complex interactions and flow dynamics within a porous medium, we aim to ensure that our model can effectively capture the elastoviscoplastic behavior in a realistic and challenging setting. This rigorous validation approach will further enhance the credibility and robustness of our computational model, providing confidence in its ability to accurately simulate and analyze elastoviscoplastic fluids in various practical applications. Before diving into the problem description and numerical investigation of fluid through porous media, let's define what porous media is.

3.3.2. Porous Media

A porous medium is defined as a solid structure, often referred to as a porous matrix, that contains interconnected voids known as pores. It is a region consisting of at least two material components, supposed to be homogenous, presenting identifiable interfaces between them, with at least one of the constituents remaining fixed or slightly deformable or simply the solid structure with interconnected voids [28]. The key properties of a porous medium consist of porosity and permeability.

3.3.3. Porosity and Permeability

Porosity is defined as the ratio of the volumes of the void to the total volume of the material. Mathematically it is written as:

$$\phi = \frac{V_p}{V_t} \tag{27}$$

where ϕ is the porosity. Here $V_t = V_p + V_s$, V_p representing the void volume, V_s as the solid material volume and V_t the total volume. The expression (27) can be rewritten as:

$$\phi = \frac{V_t - V_s}{V_t} \tag{28}$$

note that zero porosity means there is no space for flow, while non-zero porosity indicates that a material can flow. The greater the porosity, the more space there is for the material to

flow. Porosity usually varies from 0 to 1. After defining the porosity of the porous media the next important term is permeability. Permeability, represented by κ, indicates the ability of the fluid to flow through the porous medium. It depends on the distribution or connectivity of the pores, no pores space leads to non-permeability and in that case, $\kappa = 0$ means the medium is impermeable, whereas if κ is infinite it shows the medium offers no resistance to flow [30, 31, 32, 33]. The flow through the porous media is numerically treated by Darcy's law [34] which is a linear relationship between the velocity and the gradient of the pressure. This law is only valid for Newtonian fluids with low Reynolds numbers.

3.3.4. Problem Description (Symmetric and Unsymmetric case)

In this simulation, a symmetric configuration of cylinders is arranged within a square box of length 2.25 units. Four cylinders are positioned at each corner of the square, with a radius of 1 unit and with a porosity of 0.38 in a symmetric case, and three cylinders with a radius of 1 are placed on the bottom corner and upper part of the box with the same porosity 0.38. This geometry leads the elastoviscoplastic fluid to continuously experience contraction and expansion. The domain can be seen in Figure 5.

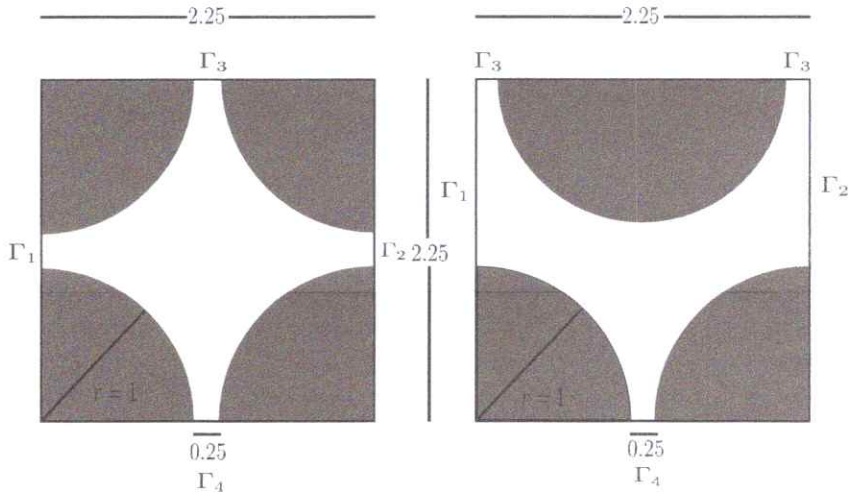

Figure 5: Computational domain for symmetric and unsymmetric porous media.

The interesting aspect of these simulations is that both the symmetric and unsymmetric arrangements of cylinders represent two extreme configurations of an ideal porous medium. In the symmetric configuration along the centerline, within a reference frame moving with the flow, the flow is nearly entirely extensional. In contrast, the unsymmetric geometry is anticipated to exhibit shear-dominated deformation nearly everywhere, and the porous media is expected to have such flow patterns [35]. To capture the yielded/unyielded region and to align our results with [9], the second invariant of the deformation tensor is observed. In the symmetric case, the domain is subjected to a velocity-driven flow entering from the left pore, while a no-slip boundary condition is enforced on the surface of the cylinder. Conversely, in the unsymmetric geometry, a pressure-driven flow is applied at the inlet, and the surface of the solid cylinders adheres to the no-slip condition. The key parameters considered in this setup include:

$$Re = \frac{\rho U r}{\eta_0}, \quad We = \frac{\lambda U}{r} \qquad \text{and} \quad Bi = \frac{\sigma_y r}{\eta_0 U} \tag{29}$$

where Re, We, and Bi denote the Reynold, Weissenberg, and Bingham numbers. Throughout the simulation, we maintain fixed Reynolds and Weissenberg numbers at 0.8 and 0.01 respectively. A sequence of simulations is conducted, varying the Bingham numbers across values of 0.1, 1, 5, and 10, while the parameter β remains constant at 0.5. This approach allows us to explore the influence of different Bingham numbers on the flow behavior while keeping other factors constant for comparative analysis. The visualization of deformation, as depicted in Figure 7 and 9, provides crucial insights into the behavior of the fluid within porous media under symmetric conditions.

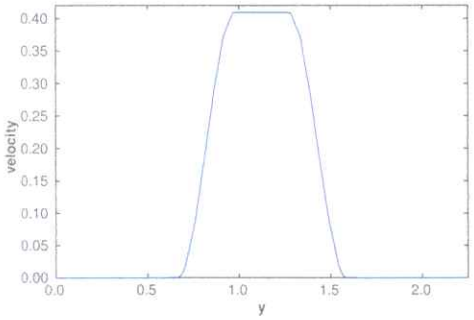

(a) Velocity cutline at the centre of domain (symmetric).

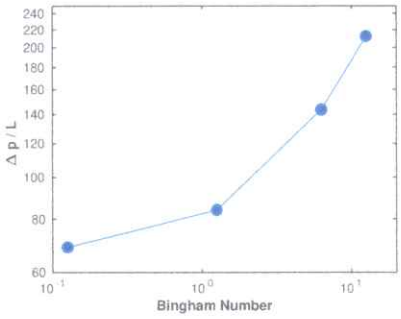

(b) Pressure drops against different Bingham numbers (symmetric).

Notably, the presence of black spots within the visual representation signifies regions of unyielding material. It is observed that as the Bingham number increases, these black regions expand in size. This observation aligns with expectations and accurately portrays the inherent characteristics of the fluid. Moreover, it's essential to note that the black region within the red moving region signifies the moving yield surface. Conversely, the black regions situated at the top and bottom of the simulation represent the static unyielded regions.

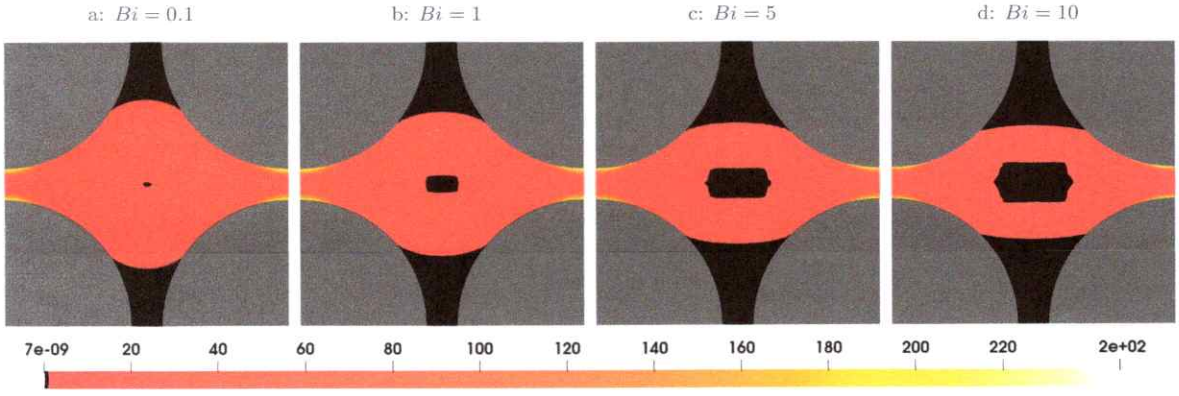

Figure 7: Visualization of the deformation in the EVP fluid within the model porous medium for the symmetric arrangement of cylinders at $Re = 0.8$, $We = 0.01$, with varying Bingham numbers.

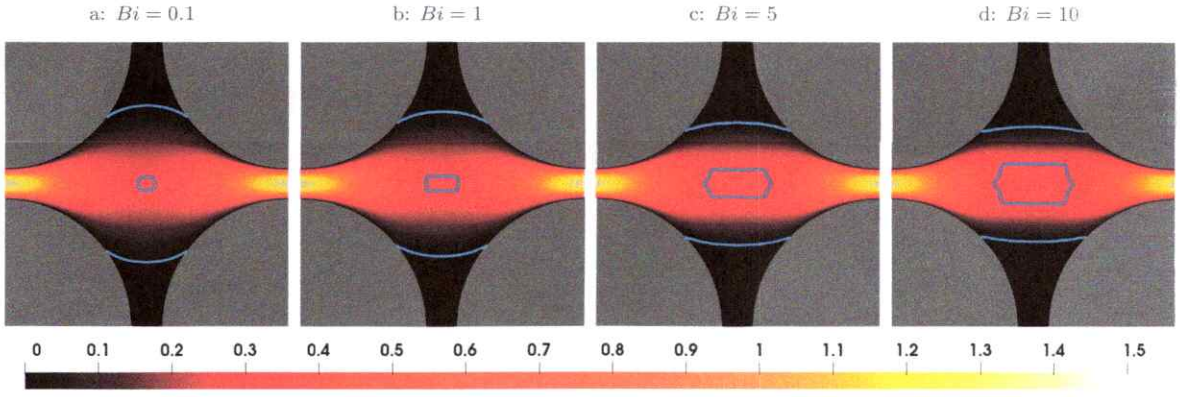

Figure 8: Visualization of the velocity contours in the EVP fluid within the model porous medium for the symmetric arrangement of cylinders at $Re = 0.8$, $We = 0.01$, with varying Bingham numbers. The blue lines in the middle represent the moving yield surfaces. The top and bottom black region is the static unyieldied region.

The blue line present in the middle in Figure 8 represents the moving yielding surface. as expected that the higher Bingham number results in the big unyielded region. The simulation we performed for the symmetric part of the porous media shows a strong agreement with the data available in the literature [9].

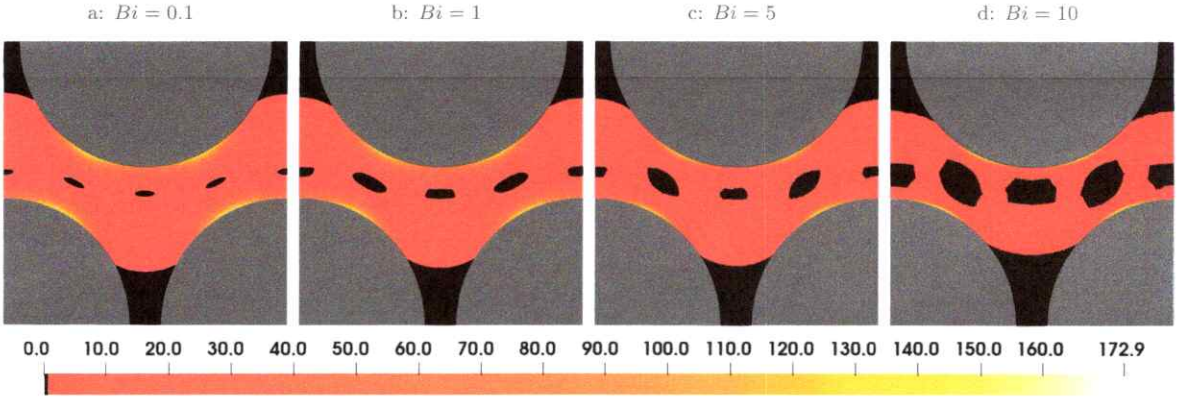

Figure 9: Visualization of the deformation in the EVP fluid within the model porous medium for the unsymmetric arrangement of cylinders at $Re = 0.8$, $We = 0.01$, with varying Bingham numbers.

The blue lines in the middle of the geometry in terms of small patterns for the unsymmetric case can be witnessed in Figure 10 represent the moving yielding surface. Like in the symmetric case the same pattern is expected for the unsymmetric part i.e., the higher the Bingham number is the bigger the unyielded region is. The top and bottom region is the static unyieldied region. The simulation for the unsymmetric part of the porous media also shows a strong agreement with reference results [9].

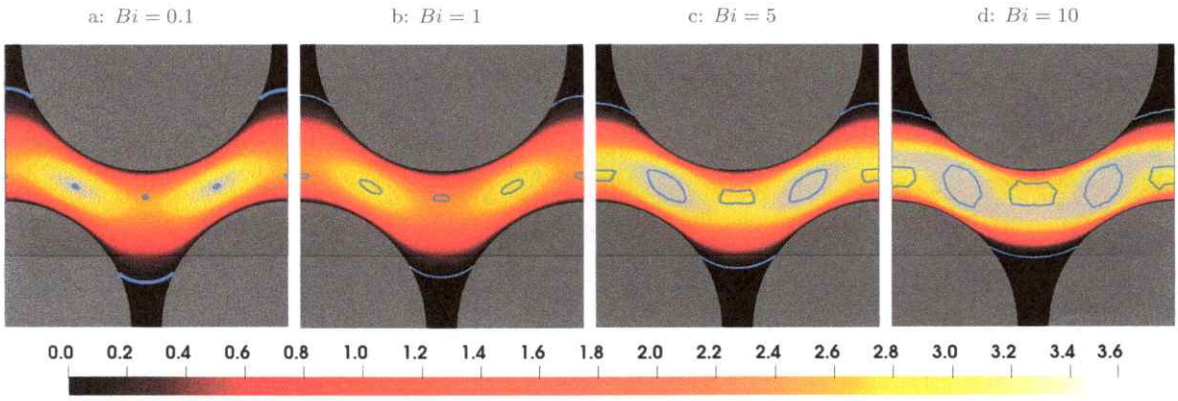

Figure 10: Visualization of the velocity contours in the EVP fluid within the model porous medium for the unsymmetric arrangement of cylinders at $Re = 0.8$, $We = 0.01$, with varying Bingham numbers. The blue lines in the middle represent the moving yield surfaces. The top and bottom black region is the static unyieldied region.

3.3.5. Flow Topology

We will now shift our focus towards the flow topology. The motivation is to figure out how the shear, rotational, and shear flow has evolved and distributed inside the symmetric and unsymmetric domains. We will achieve this with the help of a parameter Q. This parameter is known as the flow topology parameter and it is defined as:

$$Q = \frac{\mathrm{II}^2(\mathbf{D}) - \mathrm{II}^2(\mathbf{W})}{\mathrm{II}^2(\mathbf{D}) + \mathrm{II}^2(\mathbf{W})} \tag{30}$$

where $\mathrm{II}^2(\mathbf{D}) = (\mathbf{D} : \mathbf{D})$ and $\mathrm{II}^2(\mathbf{W}) = (\mathbf{W} : \mathbf{W})$. Here, $Q = -1$ corresponds to pure rotational flow, while $Q = 0$ and $Q = 1$ represent pure shear and pure elongational flow, respectively. From Figure 11 one can observe the distribution of shear, rotational, and elongational flows in the symmetric geometry of the porous medium. The figure clearly shows that shear-dominated flow occurs near the cylinder walls, rotational flow is observed at dead ends due to the presence of vortices, and the elongational pattern changes with increasing Bingham number [35].

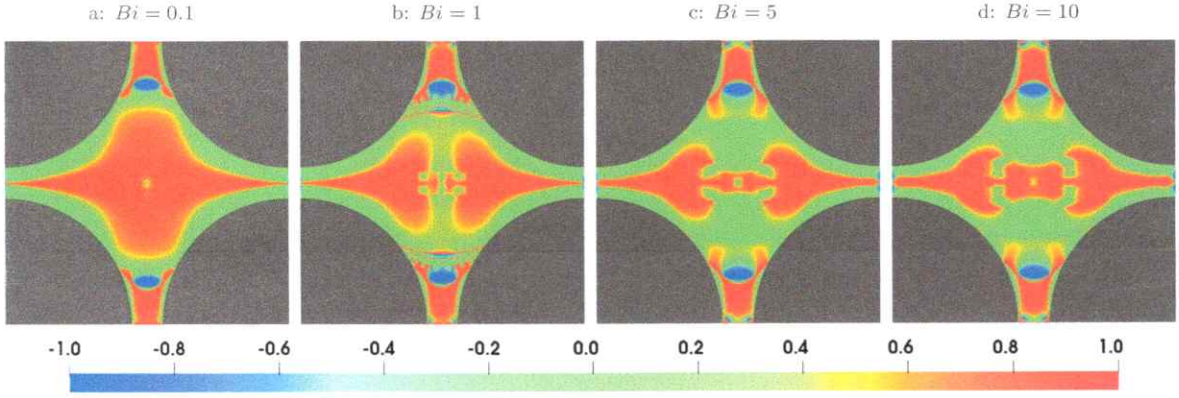

Figure 11: Visualization of the flow topology in the EVP fluid within the model porous medium.

4. Conclusion

Our current study has provided a comprehensive insight into the mathematical model for the elastoviscoplastic fluid, finite element approximation, and the behavior of fluids within different geometries including porous media. Initially, a robust mathematical framework was introduced for the elastoviscoplastic fluids, depicting the true rheological behavior of complex fluids such as elastviscoplastic fluid by incorporating the Oldroyd B model and the Papanastasiou regularized model into the momentum equation. The present mathematical model is then approximated using the finite element technique (mixed formulation) that incorporates Q_2 element for velocity stress and a discontinuous P_1 element for the approximation of pressure. To solve the resulting nonlinear system of equations arising from the finite element discretization, we applied Newton's method. This iterative approach is particularly a perfect tool for dealing with the nonlinearities inherent in elastoviscoplastic fluid behavior. The finite element framework and simulating fluid behavior through different geometries was quite challenging because of the inclusion of viscous, elastic, and plastic terms. To keep things simple and well structured we divided the numerical simulations into three parts. The first part dealt with the viscoplastic behavior of the fluid by eliminating the elastic effects. The challenge was to examine the effectiveness and convergence behavior of our numerical solver as well as to observe the optimal value of the regularization parameter to capture the viscoplastic model more accurately. The next part was to simulate the viscoelastic effects by eliminating the viscoplastic term from the mathematical model. The simulation was performed for the flow around a cylinder to find the drag over the cylinder. Our results show good agreement with the reference results. In the last part, the model was tested for viscous, plastic, and elastic terms by simulating it through a porous media with the symmetric and unsymmetric arrangement of cylinders within a domain and examining the behavior of the fluid, particularly concerning the influence of Bingham numbers. As we look ahead, our future investigations will extend beyond solely increasing the Weissenberg number. We aim to encompass a broader spectrum of Bingham numbers, ranging from small to large values. By incorporating a comprehensive range of Bingham numbers alongside higher Weissenberg numbers, we anticipate gaining a more detailed understanding of how both viscoelastic and yield stress effects interact within porous media. This expanded exploration will offer valuable insights into the complex interplay between material properties and flow dynamics. This will be done by incorporating the Bingham Papanastasiou regularized model with the other viscoelastic models, such as PTT, and FENE-P to capture the high Weissenberg number.

References

[1] P. Saramito, "A new constitutive equation for elastoviscoplastic fluid flows," *J. Non-Newtonian Fluid Mech*, vol. 145(1), pp. 1–14, 2007.

[2] P. Saramito, *Complex fluids, modeling and algorithms.* Springer, 2016.

[3] E. C. Bingham, *Fluidity and plasticity, McGraw-Hill.* New York, 1922.

[4] J. G. Oldroyd, "On the formulation of rheological equations of state," *Proceedings of*

the royal society of London. Series A, Mathematical and Physical sciences, vol. 200, pp. 523–541, 02 1950.

[5] R. J. Gordon and W. R. Schowalter, "Anisotropic fluid theory: A different approach to the dumbbell theory of dilute polymer solutions," *Transactions of The Society of Rheology*, vol. 16, pp. 79–97, 03 1972.

[6] E. D. Martynova, "Lagrangian representation of the family of Gordon–Schowalter objective derivatives at simple shear," *Moscow University Mechanics Bulletin*, vol. 75, no. 6, pp. 176–179, 2020.

[7] P. Saramito, "A new elastoviscoplastic model based on the Herschel–Bulkley viscoplastic model," *Journal of non-Newtonian Fluid Mechanics*, vol. 158, no. 1, pp. 154–161, 2009.

[8] F. Belblidia, H. Tamaddon-Jahromi, M. Webster, and K. Walters, "Computations with viscoplastic and viscoelastoplastic fluids," *Rheologica Acta*, vol. 50, pp. 343–360, 04 2011.

[9] E. Chaparian, D. Izbassarov, F. L. B. De Vita, and O. Tammisola, "Yield-stress fluids in porous media: a comparison of viscoplastic and elastoviscoplastic flows," *Meccanica*, vol. 55, no. 2, pp. 331–342, 2020.

[10] A. Bonito and E. Burman, "A continuous interior penalty method for viscoelastic flows," *SIAM Journal on Scientific Computing*, vol. 30, no. 3, pp. 1156–1177, 2008.

[11] T. C. Papanastasiou, "Flows of materials with yield," *Journal of Rheology*, vol. 31, no. 5, pp. 385–404, 1987.

[12] A. Syrakos, G. C. Georgiou, and A. N. Alexandrou, "Solution of the square lid-driven cavity flow of a Bingham plastic using the finite volume method," *Journal of Non-Newtonian Fluid Mechanics*, vol. 195, p. 19–31, May 2013.

[13] G. R. Burgos, A. N. Alexandrou, and V. Entov, "On the determination of yield surfaces in Herschel–Bulkley fluids," *Journal of Rheology*, vol. 43, pp. 463–483, 05 1999.

[14] J. Tsamopoulos, M. Chen, and A. Borkar, "On the spin coating of viscoplastic fluids," *Rheologica Acta*, vol. 35, pp. 597–615, 11 1996.

[15] T. Hughes, *The finite element method: Linear static and dynamic finite element analysis*. Dover Civil and Mechanical Engineering, Dover Publications, 2000.

[16] D. Kuzmin and J. Hämäläinen, *Finite element methods for computational fluid dynamics: A practical guide*. Philadelphia, PA: Society for Industrial and Applied Mathematics, 2014.

[17] H. Damanik, J. Hron, A. Ouazzi, and S. Turek, "Monolithic Newton-multigrid solution techniques for incompressible nonlinear flow models," *International Journal for Numerical Methods in Fluids*, vol. 71, no. 2, pp. 208–222, 2013.

[18] V. Girault and P. A. Raviart, *Finite element methods for Navier-Stokes equations*. Berlin-Heidelberg: Springer, 1986.

[19] N. Schmidt, A. Humbert, and T. Slawig, "The Newton solver with step size control is faster than the Picard iteration in simulating ice flow (FEniCS-full-Stokes v1.1.0)," *EGUsphere*, vol. 2023, pp. 1–17, 2023.

[20] J. Nordström, F. Laurén, and O. Ålund, "An explicit Jacobian for Newton's method applied to nonlinear initial boundary value problems in summation-by-parts form," *AIMS Mathematics*, vol. 9, no. 9, pp. 23291–23312, 2024.

[21] N. B. A. Ouazzi and S. Turek, "Newton-multigrid FEM solver for the simulation of quasi-Newtonian modeling of thixotropic flows," in *WCCM-ECCOMAS2020*, vol. 700 of *Numerical Methods and Algorithms in Science and Engineering*, Scipedia, 2021.

[22] A. Aposporidis, E. Haber, M. A. Olshanskii, and A. Veneziani, "A mixed formulation of the Bingham fluid flow problem: Analysis and numerical solution," *Computer Methods in Applied Mechanics and Engineering*, vol. 200, no. 29, pp. 2434–2446, 2011.

[23] A. Fatima, S. Turek, A. Ouazzi, and M. A. Afaq, "An adaptive discrete Newton method for regularization-free Bingham model," 07 2021.

[24] G. C. G. Raja R. Huilgol, *Fluid mechanics of viscoplasticity*. Springer Cham, 15 April 2022.

[25] O. M. Coronado, D. Arora, M. Behr, and M. Pasquali, "A simple method for simulating general viscoelastic fluid flows with an alternate log-conformation formulation," *Journal of non-Newtonian Fluid Mechanics*, vol. 147, no. 3, pp. 189–199, 2007.

[26] H. Damanik, J. Hron, A. Ouazzi, and S. Turek, "A monolithic FEM approach for the log-conformation reformulation (LCR) of viscoelastic flow problems," *Journal of Non-Newtonian Fluid Mechanics*, vol. 165, no. 19, pp. 1105–1113, 2010.

[27] S. Wittschieber, L. Demkowicz, and M. Behr, "Stabilized finite element methods for a fully-implicit logarithmic reformulation of the Oldroyd-B constitutive law," *Journal of Non-Newtonian Fluid Mechanics*, vol. 306, p. 104838, 2022.

[28] Z. Heinemann and G. Mittermeir, *Fluid flow in porous media*. PHDG textbook series, PHDG, 2 ed., Feb. 2013.

[29] H. J. Seybold, U. Eberhard, E. Secchi, R. L. C. Cisne, J. Jiménez-Martínez, R. F. S. Andrade, A. D. Araújo, M. Holzner, and J. Andrade, "Localization in flow of non-Newtonian fluids through disordered porous media," *Frontiers in Physics*, vol. 9, 2021.

[30] F. De Vita, M. Rosti, D. Izbassarov, L. Duffo, O. Tammisola, S. Hormozi, and L. Brandt, "Elastoviscoplastic flows in porous media," *Journal of Non-Newtonian Fluid Mechanics*, vol. 258, pp. 10–21, 2018.

[31] F. Durst, R. Haas, and W. Interthal, "The nature of flows through porous media," *Journal of Non-Newtonian Fluid Mechanics*, vol. 22, no. 2, pp. 169–189, 1987.

[32] I. F. Macdonald, M. S. El-Sayed, K. Mow, and F. A. L. Dullien, "Flow through porous media-the Ergun equation revisited," *Industrial & Engineering Chemistry Fundamentals*, vol. 18, no. 3, pp. 199–208, 1979.

[33] T. Sochi, "Non-Newtonian flow in porous media," *Polymer*, vol. 51, no. 22, pp. 5007–5023, 2010.

[34] A. Verruijt, *Darcy's Law*, pp. 6–13. London: Macmillan Education UK, 1970.

[35] S. De, J. A. M. Kuipers, E. A. J. F. Peters, and J. T. Padding, "Viscoelastic flow simulations in model porous media," *Phys. Rev. Fluids*, vol. 2, p. 053303, May 2017.